## **Inorganic Chemistry**

pubs.acs.org/IC Article

# Structure and Characterization of K<sub>2</sub>Na<sub>3</sub>B<sub>2</sub>P<sub>3</sub>O<sub>13</sub>, a New Nonlinear Optical Borophosphate with One-Dimensional Chain Structure and Short Ultraviolet Cutoff Edge

Wenhao Liu, Ming-Hsien Lee, Ruixin Guo, and Jiyong Yao\*



Cite This: Inorg. Chem. 2023, 62, 2480-2488



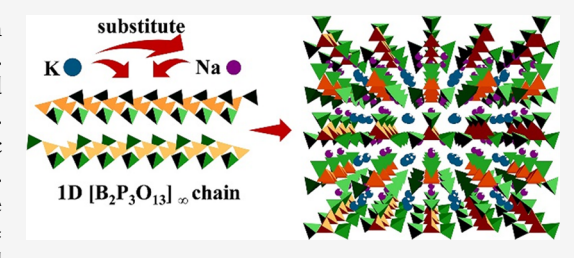
**ACCESS** I

III Metrics & More

Article Recommendations

**Supporting Information** 

**ABSTRACT:** Nonlinear optical (NLO) crystals, being the primary medium for laser wavelength conversion, are crucial in all-solid-state lasers. Borophosphates offer more structural varieties than pure borates and phosphates, and they have become popular as NLO crystal candidates. Through spontaneous crystallization, we acquired a noncentrosymmetric alkali metal borophosphate crystal material,  $K_2Na_3B_2P_3O_{13}$  (KNBPO). KNBPO crystallizes in the orthorhombic  $Cmc2_1$  space group with the following unit cell parameters: a = 13.9238(18) Å, b = 6.7673(8) Å, c = 12.1298(15) Å, and C = 4, and its structure is characterized by a fundamental



building unit  $1_{\infty}$  [B<sub>2</sub>P<sub>3</sub>O<sub>13</sub>] chain structure made up of bridging oxygen linkages between BO<sub>4</sub> and PO<sub>4</sub> tetrahedra. KNBPO has a short ultraviolet (UV) cut-off edge (<186 nm), a congruent melting characteristic, good thermal stability, and a moderate second harmonic generation response roughly 0.42 times that of KH<sub>2</sub>PO<sub>4</sub>. Theoretical calculations reveal that the optical properties of the compound mainly originate from BO<sub>4</sub> and PO<sub>4</sub> units. Due to the short UV cut-off edge, KNBPO can be used as a potential NLO material in the UV and even deep UV regions, and it enhances the structural variety of borophosphates, which has a reference value for scholars investigating similar materials.

#### INTRODUCTION

As one of the four greatest innovations of the 20th century, laser technology has become an integral part of people's everyday lives. <sup>1–3</sup> Nonlinear optical (NLO) crystals, as crucial materials that could extend the laser wavelength, have also attracted a growing amount of scientific attention. 4-8 Through the unremitting efforts of scientists, some NLO crystal materials with excellent comprehensive properties and commercial value have been discovered, which primarily include borate and phosphate crystal materials, such as KBe<sub>2</sub>BO<sub>3</sub>F<sub>2</sub> (KBBF), LiB<sub>3</sub>O<sub>5</sub> (LBO),  $\beta$ -BaB<sub>2</sub>O<sub>4</sub> (BBO), CsB<sub>3</sub>O<sub>5</sub> (CBO), CsLiB<sub>6</sub>O<sub>10</sub> (CLBO), KH<sub>2</sub>PO<sub>4</sub> (KDP), KTiOPO<sub>4</sub> (KTP), NH<sub>4</sub>H<sub>2</sub>PO<sub>4</sub> (ADP), etc.<sup>9-18</sup> These wellknown crystalline materials are limited in practical production applications to varying degrees due to inherent defects such as the highly toxic raw material Be and its severe layered growth habit of KBBF, the two-photon absorption and photorefraction of BBO, the serious deliquescence of CLBO, and the incompatibility with realistic laser output below 355 nm of KDP, KTP, and ADP. In practice, exploration of novel ultraviolet (UV) NLO materials has significant scientific value in contemporary culture.

Borophosphates are heterogeneous substances that combine borates and phosphates but are distinct from them.  $^{19-21}$  Three-coordinated planar triangle BO<sub>3</sub> and four-coordinated tetrahedral BO<sub>4</sub> are the predominant coordination modes of B in borate materials.  $^{22}$  These two types of B–O units may also

be joined to form B<sub>3</sub>O<sub>6</sub>, B<sub>3</sub>O<sub>7</sub>, and B<sub>5</sub>O<sub>10</sub>, among others. <sup>10,11,23–26</sup> Phosphates primarily include four-coordinated tetrahedral PO<sub>4</sub>, and PO<sub>4</sub> can also be polycondensed into oligomeric groups such as P<sub>2</sub>O<sub>7</sub>, P<sub>3</sub>O<sub>10</sub>, P<sub>4</sub>O<sub>13</sub>, etc. that are connected by corner share. <sup>27–32</sup> The primary distinction between borophosphates and pure borates and phosphates is that the structure of borophosphates ought to have B–O–P bonds connected by bridging oxygens. Correspondingly, borophosphates exhibit a richer structural chemistry variety than borates and phosphates. Kniep and co-workers categorized borophosphates systematically from the perspective of structural chemistry, chiefly based on the boron-to-phosphorus ratio and the varied fundamental building units (FBUs) of anionic groups in the structure, giving us a better knowledge of borophosphates. <sup>20</sup>

Borophosphates have a variety of properties due to their complex structures. <sup>33</sup> Nevertheless, researchers have discovered that noncentrosymmetric structures are not the norm in borophosphates, <sup>34</sup> and only a few compounds, such as  $BPO_4$ ,  $MBPO_5$  (M = Ca, Sr, Ba),  $KMBP_2O_8$  (M = Sr, Ba),

Received: December 24, 2022 Published: January 25, 2023





 $\begin{array}{lll} Na_5B_2P_3O_{13}, & MPbBP_2O_8 \ (M=K,\ Rb),\ Na_3Cd_3BP_4O_{16},\ etc.,\\ exhibit & NLO & properties. \end{array}$ considered a promising deep UV NLO material due to its short deep UV cut-off edge, large nonlinear coefficient, and high laser damage threshold. Since the BPO<sub>4</sub> structure contains only tetrahedral groups BO<sub>4</sub> and PO<sub>4</sub>, its birefringence is small, which limits its phase-matching ability. However, being the first borophosphate NLO crystal material identified, BPO<sub>4</sub> has caught the interest of borophosphate researchers. 43-45 For the investigation of novel NLO materials, second-order Jahn-Teller (SOJT) groups can be inserted into the NLO active groups to increase the NLO performance of the materials, such as  $Pb_2B_5O_9I$  and  $Cd_4BiO(BO_3)_3$ . It was discovered, however, that the addition of SOJT groups red-shifted the cut-off edge, which was incompatible with the short cut-off edge. 48 In order to find UV NLO materials with excellent comprehensive properties, it is a prerequisite for the material itself to have UV transmission. To preserve the excellent optical transmission of borophosphate NLO active groups BO<sub>3</sub>, BO<sub>4</sub>, and PO<sub>4</sub>, it is acceptable to incorporate into the structure alkali metals, alkaline earth metals, and rare-earth elements with fully closed-shell electronic structures, which lack d-d and f-f electronic transitions.

Following the principles above, we focus on the exploration of alkali metal borophosphates. Two related compounds, Na<sub>5</sub>B<sub>2</sub>P<sub>3</sub>O<sub>13</sub><sup>39</sup> and KNa<sub>4</sub>B<sub>2</sub>P<sub>3</sub>O<sub>13</sub>,<sup>42</sup> were discovered by previous researchers in the study of alkali metal borophosphates. Although the two compounds have similar crystal structures, they crystallize in different space groups (P21 for Na<sub>5</sub>B<sub>2</sub>P<sub>3</sub>O<sub>13</sub> and Pna2<sub>1</sub> for KNa<sub>4</sub>B<sub>2</sub>P<sub>3</sub>O<sub>13</sub>), and the second harmonic generation (SHG) response of Na<sub>5</sub>B<sub>2</sub>P<sub>3</sub>O<sub>13</sub> is larger than that of KNa<sub>4</sub>B<sub>2</sub>P<sub>3</sub>O<sub>13</sub>. In this research, we aimed to investigate how structures and properties change with increasing K content of compounds in the KxNa5-xB2P3O13 (x = 0, 1, 2, 3, 4, and 5) system. In this research, we identified a noncentrosymmetric borophosphate substance K<sub>2</sub>Na<sub>3</sub>B<sub>2</sub>P<sub>3</sub>O<sub>13</sub> (KNBPO) via high-temperature spontaneous crystallization. KNBPO has a short UV cut-off edge as well as an appropriate SHG response. The crystal structure, thermal characteristics, optical properties, and electronic structure of KNBPO are all described in depth in this paper.

#### **■ EXPERIMENTAL SECTION**

Crystal Growth of KNBPO. A spontaneous crystallization procedure utilizing NH<sub>4</sub>BF<sub>4</sub> (99.5%, Aladdin) flux was used to generate single crystal samples of  $K_xNa_{5-x}B_2P_3O_{13}$  (x = 2, 3, 4, and 5). The raw components and flux were mixed in an agate mortar (molar ratio of  $K_2CO_3-Na_2CO_3-B_2O_3-NH_4H_2PO_4-NH_4BF_4 = 2:3:2:6:3$ for x = 2,  $K_2CO_3 - Na_2CO_3 - B_2O_3 - NH_4H_2PO_4 - NH_4BF_4 = 3:2:2:6:3$ for x = 3,  $K_2CO_3 - Na_2CO_3 - B_2O_3 - NH_4H_2PO_4 - NH_4BF_4 = 4:1:2:6:3$ for x = 4, and  $K_2CO_3 - B_2O_3 - NH_4H_2PO_4 - NH_4BF_4 = 5:2:6:3$  for x = 45) before being transferred to platinum crucibles. The initial mixed samples were fully melted by heating the crystal growth furnace to 700 °C at a rate of 1 °C/min and keeping them at this temperature for 24 h. The samples were then cooled to 300  $^{\circ}$ C at a rate of 1  $^{\circ}$ C/h and then brought down to room temperature at a rate of 20  $^{\circ}\text{C/h}.$ Finally, only the sample with x = 2 had transparent crystals in the platinum crucible. In platinum crucibles of samples with  $3 \le x \le 5$ , we found that the obtained compounds were very prone to hygroscopic decomposition (within ten minutes), indicating that the K tolerance in the  $K_xNa_{5-x}B_2P_3O_{13}$  system is x=2. Synthesis of the Polycrystalline Powder Sample. The

**Synthesis of the Polycrystalline Powder Sample.** The polycrystalline powder samples of  $K_xNa_{5-x}B_2P_3O_{13}$  (x=0,1, and 2) were synthesized by the traditional high-temperature solid-state reaction method. The raw materials for the initial reaction included

 $K_2CO_3$  (99%, Aladdin),  $Na_2CO_3$  (99%, Aladdin),  $B_2O_3$  (98%, Aladdin), and  $NH_4H_2PO_4$  (99%, Aladdin). The reaction raw materials for  $K_xNa_{5-x}B_2P_3O_{13}$  ( $x=0,\ 1,\ and\ 2)$  were accurately weighed according to the stoichiometric ratio and mixed evenly in an agate mortar. The ground mixed raw materials were put in platinum crucibles and pre-fired at 550 °C for 24 h in a muffle furnace in order to completely volatilize impurities such as  $NH_3$  and  $CO_2$  in the mixed raw materials. The pre-fired samples were crushed in agate, followed by complete grinding. The pre-fired samples were then put in platinum crucibles and sintered at 600 °C (for KNBPO), 650 °C (for  $KNa_4B_2P_3O_{13}$ ), and 680 °C (for  $Na_5B_2P_3O_{13}$ ) for 24 h in a muffle furnace, respectively. During the synthesis of  $K_xNa_{5-x}B_2P_3O_{13}$  (x=0,1,1) and 2) polycrystalline powder samples, the muffle furnace's heating and cooling speeds were both 1 °C/min. For further characterization, the sintered samples were eventually crushed to fine powder.

**Structure Determination.** Data for single crystal X-ray diffraction on transparent bulk crystal KNBPO was acquired using a Rigaku AFC10 diffractometer equipped with graphite monochromatic Mo-K $\alpha$  ( $\lambda$  = 0.71073 Å) radiation at 293 K. For data collection and absorption correction, the CrysAlispro program and the multi-scan technique have been used. The crystal structure of KNBPO was solved with the SHELXT<sup>49</sup> solution program using the dual method and using Olex2 1.3<sup>50</sup> as the graphical interface, and the structure refinement of the model KNBPO was performed with SHELXL<sup>51</sup> 2014/7 using full matrix least squares minimization on  $F^2$ . Table 1

Table 1. Crystallographic Data and Structure Refinements for KNBPO

```
formula weight
                                        469.70
temperature/K
                                        296.15
crystal system
                                        orthorhombic
space group
                                        Cmc2<sub>1</sub>
a/Å
                                        13.9238(18)
b/Å
                                        6.7673(8)
c/Å
                                        12.1298(15)
\alpha/^{\circ}
                                        90
β/°
                                        90
\gamma/^\circ
                                        90
volume/Å3
                                        1142.9(2)
\rho_{\rm calc}/{\rm g/cm^3}
                                        2.730
\mu/\text{mm}^{-1}
                                        1.440
F(000)
                                        920.0
radiation
                                        Mo K\alpha (\lambda = 0.71073)
2\theta range for data collection/°
                                        5.852 to 66.264
index ranges
                                        -21 \le h \le 21, -9 \le k \le 10, -18 \le l \le 10
reflections collected
independent reflections
                                        1837 [R_{\text{int}} = 0.0437, R_{\text{sigma}} = 0.0541]
data/restraints/parameters
                                        1837/1/117
goodness-of-fit on F2
                                        1.067
final R indexes [I > = 2\sigma(I)]
                                        R_1 = 0.0490, wR_2 = 0.1181^a
final R indexes [all data]
                                        R_1 = 0.0691, wR_2 = 0.1296^a
largest diff. Peak/hole/e Å<sup>-3</sup>
                                        0.55/-0.94
Flack parameter
                                        0.24(15)
{}^{a}R_{1} = \Sigma ||F_{0}| - |F_{c}||/\Sigma |F_{0}|, and wR_{2} = [\Sigma w(F_{0}^{2} - F_{c}^{2})^{2}/\Sigma wF_{0}^{4}]^{1/2} for
F_0^2 > 2\sigma (F_0^2).
```

lists crystallographic parameters for KNBPO. Tables S1 and S2 show the exact atomic coordinates and equivalent isotropic temperature factors and specified bond lengths of KNBPO, respectively.

**Characterization of the Powder Sample.** The polycrystalline powder sample KNBPO was analyzed at room temperature using a Bruker D8 X-ray diffractometer equipped with a Cu K $\alpha$  ( $\lambda$  = 1.540598 Å) radiation source. For the sample characterization, the scanning step length was 0.02° and the scanning rate was 0.1 s/step.

Powder X-ray diffraction (PXRD) data with a  $2\theta$  range of  $10^{\circ}$  to  $80^{\circ}$  was acquired.

**Optical Characterizations.** The diffuse reflectance spectrum of the powder KNBPO sample in the 186–2500 nm range was measured using a Shimadzu UV-3600 PLUS UV-vis-NIR spectrometer and BaSO<sub>4</sub> as a reference. In the region of 400–2000 cm<sup>-1</sup>, an Excalibur 3100 Fourier transform infrared (IR) spectrometer was used to characterize the IR spectra of the powder KNBPO sample. The KNBPO powder was thoroughly crushed with KBr (99%, Aladdin) powder at a mass ratio of 1:100 to prepare the sample for infrared measurement.

**Thermal Measurements.** NETZSCH STA 2500 was used to measure differential scanning calorimetry (DSC) and thermogravimetric (TG) testing of KNBPO. The 10 mg samples were placed in a platinum crucible and heated to 800 °C under the following test conditions:  $N_2$  atmosphere, 10 °C/min heating rate, and 10 °C/min cooling rate.

**Powder SHG Measurement.** For KNBPO powder SHG experiments, the Kurtz and Perry approach was used. <sup>52</sup> A Q-switched Nd: YAG laser with a wavelength of 1064 nm was used for the process. KNBPO samples of different particle sizes (50–100, 100–150, 150–200, 200–250, and 250–300  $\mu$ m) were obtained by grinding and filtering their crystalline samples. The crystalline KDP sample (99%, Aladdin) used as a reference was also pulverized into the same particle sizes as the KNBPO above for testing.

**Elemental Analysis.** The elemental distributions of KNBPO are determined using energy-dispersive X-ray spectroscopy. To acquire elemental mapping images, a field emission scanning electron microscope (SEM, S-4300, Hitachi) with an accelerating voltage of 15 kV was used. Due to the large deviation of the element analysis results of the two light elements, B and O, the contents of the heavy elements K, Na, and P were characterized. Figure S1 illustrates the heavy elements' specific content and distribution results.

Computational Methods. The first-principles calculations for the KNBPO crystal are performed by the plane-wave pseudopotential method implemented in the CASTEP package based on the density functional theory (DFT). 53-56 The exchange-correlation functional was chosen to be the Perdew-Burke-Ernzerhof (PBE) functional within the generalized gradient approximation (GGA).<sup>57</sup> The planewave energy cutoff was set as 750 eV and the self-consistent-field tolerance was set as  $10^{-6}$  eV/atom. The Monkhorst-Pack k-point sampling mesh density of 0.08 Å<sup>-1</sup> separation over the Brillouin zone was chosen for the primitive unit cell.<sup>58</sup> The optimized normconserving pseudopotentials<sup>59</sup> in the Kleinman-Bylander<sup>60</sup> form are used to describe the effective interaction between atom cores and valence electrons for all the elements. The distribution of valence electrons for each element in KNBPO are K 3s<sup>2</sup>3p<sup>6</sup>4s<sup>1</sup>, Na 2s<sup>2</sup>2p<sup>6</sup>3s<sup>1</sup>, B 2s<sup>2</sup>2p<sup>1</sup>, P 3s<sup>2</sup>3p<sup>3</sup>, and O 2s<sup>2</sup>2p<sup>4</sup>. Based on the experimentally obtained crystal structure, the electronic band structure of KNBPO was calculated. The SHG coefficient  $d_{ii}$  was calculated using the density functional perturbation theory, recently implemented in CASTEP.61,62

#### **■ RESULTS AND DISCUSSION**

**PXRD Data.** KNBPO single crystals were grown employing the high-temperature molten salt spontaneous crystallization technique, and its crystal structure was determined using single crystal structure analysis. To assess the plausibility of the solved crystal structural model, we preliminarily synthesized polycrystalline powder samples using a conventional high-temperature solid-state method. As illustrated in Figure 1, the experimental PXRD pattern agreed with the calculated pattern based on single-crystal crystallographic data, and simultaneous PXRD analysis validated the phase purity of KNBPO.

**Crystal Structure.** KNBPO has a noncentrosymmetric structure and it crystallizes in the orthorhombic space group  $Cmc2_1$  (No. 36), with the asymmetric unit containing one K, two Na, two B, two P, and eight O. These atoms occur in the

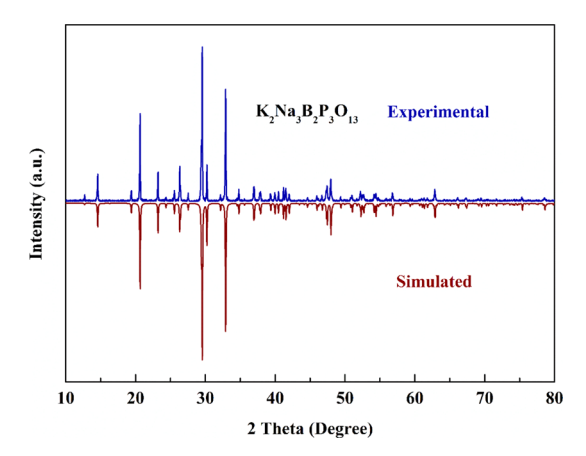


**Figure 1.** Comparison of experimental polycrystalline powder and theoretically simulated PXRD patterns of KNBPO.

structure as the coordinated forms of  $KO_8$ ,  $Na1O_6$ ,  $Na2O_{10}$ ,  $BO_4$ , and  $PO_4$ , respectively. The basic building units (BBUs) of KNBPO are made up of  $BO_4$  and  $PO_4$  tetrahedra that are joined together by shared bridging oxygen, with B:P ratios of 1:1 and 1:2, respectively (Figure 2a). The B–O bonds in the

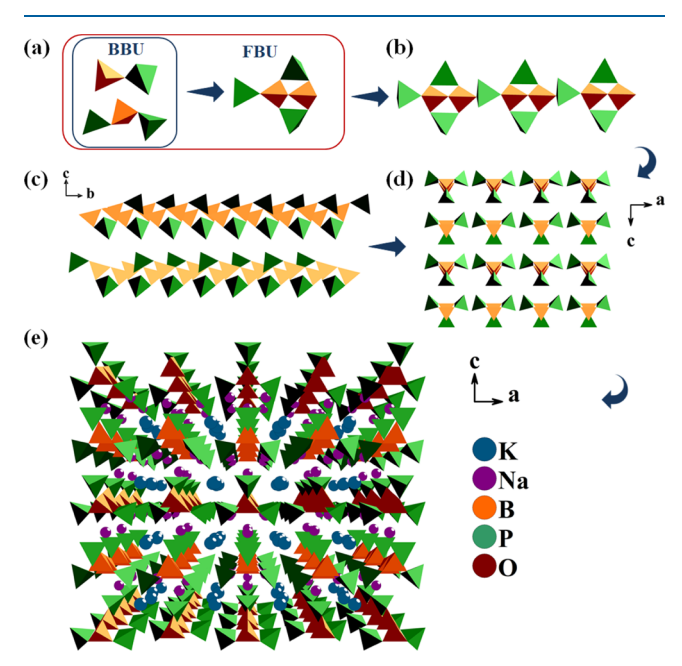


Figure 2. (a) BBU and FBU composed of BO<sub>4</sub> and PO<sub>4</sub> units in the KNBPO structure. (b)  $1_{\infty}$  [B<sub>2</sub>P<sub>3</sub>O<sub>13</sub>] is built from the condensation of the FBU [B<sub>2</sub>P<sub>3</sub>O<sub>13</sub>]. (c) Reverse alignment of adjacent  $1_{\infty}$  [B<sub>2</sub>P<sub>3</sub>O<sub>13</sub>] chains along the *b*-axis. (d) Backbone structure of KNBPO is made up of adjacent  $1_{\infty}$  [B<sub>2</sub>P<sub>3</sub>O<sub>13</sub>] chain layers arranged along the *b*-axis in opposing orientations. (e) 1D virtually unlimited  $_{\infty}$  [B<sub>2</sub>P<sub>3</sub>O<sub>13</sub>] chain structure in KNBPO.

 $BO_4$  tetrahedron possess bond lengths ranging from 1.427(10) to 1.485(7) Å with an average bond length of 1.467 Å. Similarly, the bond lengths of P–O bonds in PO<sub>4</sub> tetrahedra vary between 1.475(5) and 1.582(7) Å with an average of 1.526 Å. Borophosphates are heterostructured phosphate-borate compounds, and the ratio of BBU BO<sub>4</sub> to PO<sub>4</sub> in the structure is one of the most significant categorization criteria for borophosphates since it has a large impact on the structural arrangement of anionic groups. To minimize P–O–P bond formation, the ratio of different anionic groups in borophos-

phates should be oriented toward B:P  $\leq$  1:1, which is more advantageous for phosphate groups to occupy terminal positions. The FBU in KNBPO is a B<sub>2</sub>P<sub>3</sub>O<sub>13</sub> group generated via the polycondensation of several forms of BBUs constituted of BO<sub>4</sub> and PO<sub>4</sub>. The FBU with B:P = 2:3 can be viewed as a group of five tetrahedra linked by two types of BBUs (B:P = 1:1 and B:P = 1:2) via sharing bridging oxygen (Figure 2a). Each FBU is joined in an ordered fashion and extends parallel to the *b*-axis to produce a  $1_{\infty}$  [B<sub>2</sub>P<sub>3</sub>O<sub>13</sub>] chain. Viewed from the c-axis direction, two adjacent  $1_{\infty}$  [B<sub>2</sub>P<sub>3</sub>O<sub>13</sub>] chains are staggered and arranged in parallel along the b-axis direction. The  $1_{\infty}$  [B<sub>2</sub>P<sub>3</sub>O<sub>13</sub>] chain layers on the neighboring ab planes are placed forward and backward along the b-axis direction in the structure (Figure 2b-d). As illustrated in Figure 2e, K and Na chains are packed into the one-dimensional anion backbone along the b-axis in an orderly manner, and finally, a one-dimensional KNBPO spatial structure with asymmetric centers is formed. KNBPO has a similar FBU group and a  $1_{\infty}$  $[B_2P_3O_{13}]$  chain compared to its related compounds  $Na_5B_2P_3O_{13}^{\phantom{13}39}$  and  $KNa_4B_2P_3O_{13}^{\phantom{13}42}$  With the increase of the K content from  $Na_5B_2P_3O_{13}$  to  $KNa_4B_2P_3O_{13}$  and to KNBPO, the distortion of the  $1_{\infty}$  [B<sub>2</sub>P<sub>3</sub>O<sub>13</sub>] chain in their  $1_{\infty}$  [B<sub>2</sub>P<sub>3</sub>O<sub>13</sub>] chain-layer skeleton structure is reduced (Figure S2), and the symmetry of the space group is further improved, so that they crystallize in the monoclinic P21, orthorhombic Pna21, and orthorhombic Cmc21 space groups, respectively.

**Thermal Stability.** To explore the melting point of KNBPO and whether it is a congruently melting compound, we performed DSC characterization (Figure 3). The DSC

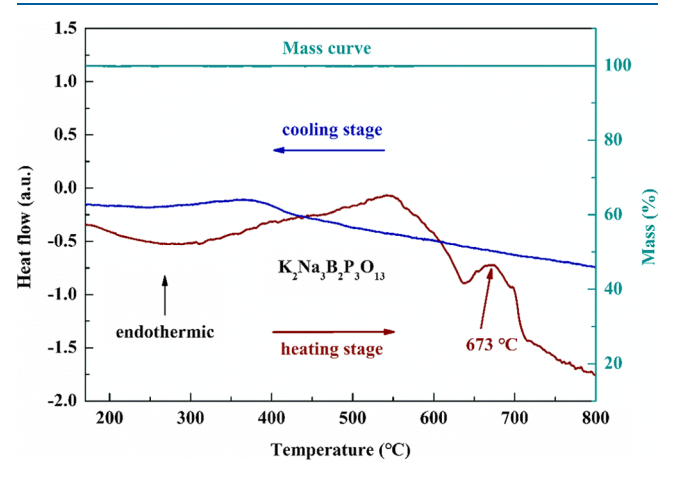


Figure 3. DSC and TG curves of KNBPO.

curve reveals a broad peak at about 530 °C in the heating stage, followed by a clear endothermic peak around 673 °C. The polycrystalline powder synthesis of KNBPO is through the two processes of pre-sintering at 550 °C and sintering at 600 °C, in which the state of KNBPO is solid. The PXRD results in Figure 1 show that the sample synthesized at 600 °C is the KNBPO pure phase, indicating that the broad peak near 530 °C in Figure 3 is not the real endothermic peak of the sample but the background peak in the instrumental characterization process. We observed the state of the KNBPO sample while it was gently heated up to further identify the melting point peak of KNBPO. The findings demonstrate that the sample is solid before 673 °C and quickly melts into a liquid after the temperature reaches 673 °C, which phenomenon corresponds to the endothermic peak at 673 °C in the DSC curve, implying

that the melting point of KNBPO is 673 °C. Strangely, no obvious exothermic peak was observed during the cooling stage, which means that the exact freezing point temperature of KNBPO cannot be obtained from the present DSC data alone. During the crystal growth experiment, we discovered that if the cooling rate of growing KNBPO crystals is too quick, the molten sample will easily become a glassy sample analogous to clear glass. As a consequence, it is speculated that rapid cooling of the instrument during DSC characterization makes the sample glassy rather than crystalline, resulting in no visible exothermic peak during the cooling process in the DSC data, which also occurs in the boron-rich systems and other borophosphates. 23,63 In order to further confirm whether KNBPO is a congruent melting compound, we heated the KNBPO polycrystalline powder to melt and then cooled it to room temperature at a cooling rate of 0.5 °C/h and performed the PXRD test. Although the PXRD patterns of KNBPO before and after melting appear to have a preferred orientation due to different crystal plane reflection intensities, it is still the same phase before and after melting, indicating that it is a congruent melting compound, as shown in Figure S3. This finding is also observed in the related congruent melting compounds Na<sub>5</sub>B<sub>2</sub>P<sub>3</sub>O<sub>13</sub> and KNa<sub>4</sub>B<sub>2</sub>P<sub>3</sub>O<sub>13</sub> (Figures S4 and S5). The TG curve corresponding to the right axis of Figure 3 illustrates that there is almost negligible weight loss of KNBPO during the temperature range of the measurement, implying that it has good thermal stability.

**Optical Properties.** The UV-vis-NIR diffuse reflectance spectrum of Figure 4a demonstrates that KNBPO has a high reflectance in the broad range of 400–2500 nm. Due to the presence of alkali metals in its structure, there are no d-d and f-f electronic transitions affecting transmission in KNBPO. Finally, KNBPO still maintains a reflection intensity of 40.25% at 186 nm, indicating that its UV cut-off edge is less than 186 nm. Therefore, KNBPO may have potential applications in the UV and even deep UV regions.

Considering that the IR spectrum can deduce the molecular structure of substances from information such as relative vibrations and molecular rotations between atoms inside the molecule, we can use it to investigate the unique coordination environment of B and P in the structure. Figure 4b illustrates that the characteristic absorption peaks of the IR spectrum of KNBPO are mostly concentrated in the fingerprint region and have a peak shape similar to the borophosphates reported by Chen and co-workers.<sup>64</sup> The absorption peak at 1039 cm<sup>-1</sup> corresponds to the BO4's asymmetric stretching vibration. The absorption peaks around 916, 870, 827, and 750 cm<sup>-1</sup> are the outcome of BO4's symmetric stretching vibration. PO4 is responsible for the asymmetric stretching vibration peak of about 1099 cm<sup>-1</sup>. The peak of the symmetric stretching vibration of PO<sub>4</sub> is around 985 cm<sup>-1</sup>. The bending vibration peaks of the BO<sub>4</sub> and PO<sub>4</sub> groups are found below 680 cm<sup>-1</sup>. The coordination modes and structures of B and P that correspond to the absorption peak data in the IR spectrum are tetra-coordinated tetrahedral groups. This conclusion is consistent with the findings of other studies and also corresponds to the crystal structure that we solved.

**SHG Properties.** The variation of the SHG intensity response of different particle sizes characterized by the Kurtz and Perry method is shown in Figure 5a. Similar to the change trend of the KDP curve, the SHG intensity of the KNBPO curve also grows consistently with the particle size, indicating that it can achieve type-I phase matching at 1064 nm

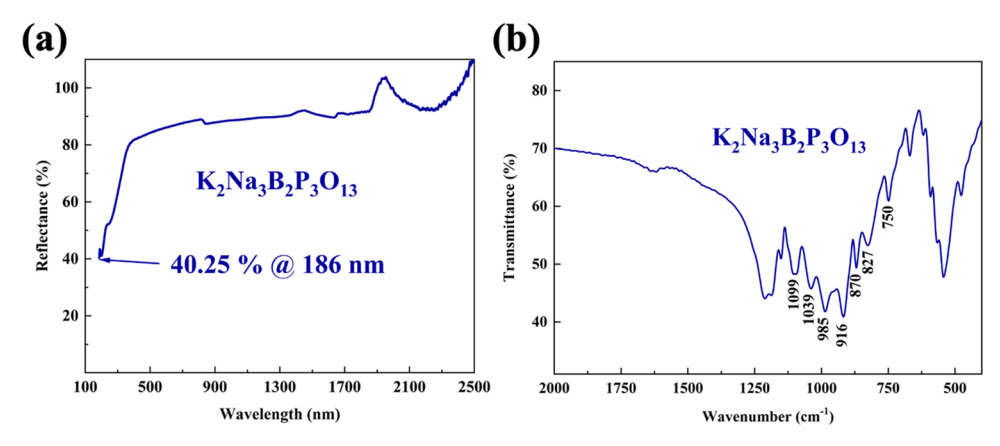


Figure 4. (a) UV-vis-NIR diffuse reflectance spectrum of powder KNBPO. (b) IR spectrum of KNBPO powder.

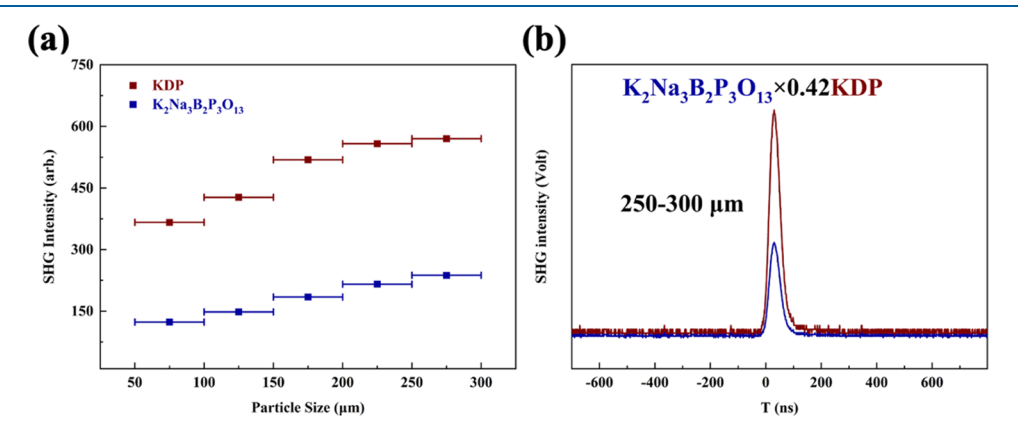


Figure 5. (a) SHG intensity curve with different particle sizes and (b) SHG intensity curves with a single particle size of KNBPO.

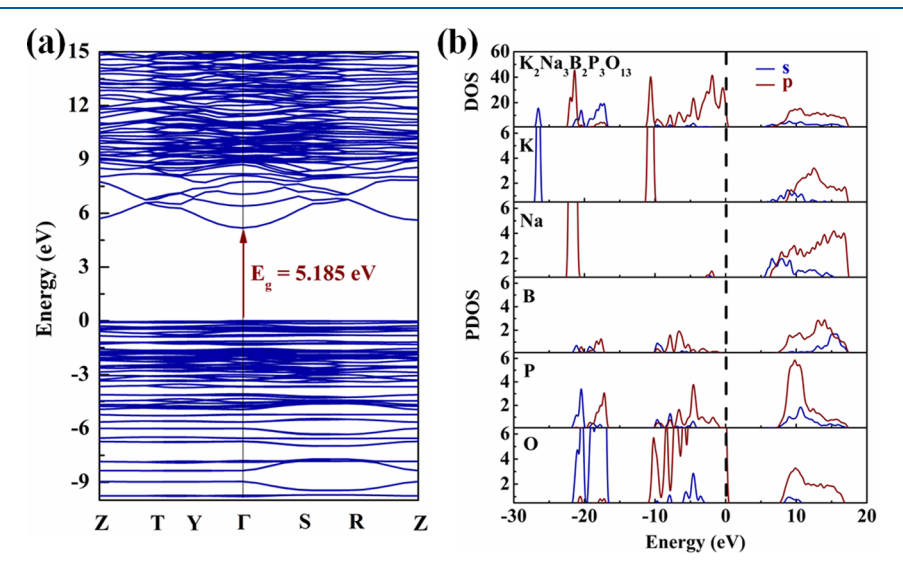


Figure 6. (a) Calculated electronic energy band structure; (b) DOS and PDOS of the KNBPO.

wavelength laser. According to the SHG single particle size intensity curve shown in Figure 5b, the SHG response intensity of KNBPO is about 0.42 times that of KDP in the range of  $250-300~\mu m$ . Compared to its related compounds  $Na_5B_2P_3O_{13}$  and  $KNa_4B_2P_3O_{13}$ , when the K content in the structure increases, the distortion of their respective  $1_\infty$   $[B_2P_3O_{13}]$  chain gradually diminishes, and the microscopic polarizability in the structure decreases as well, resulting in a lower macroscopic SHG response (in the same particle size).  $^{39,42}$  The anionic group theory proposed by Chen et

al. <sup>65</sup> points out that the B–O groups make a major contribution to the SHG response of borates, where the non- $\pi$ -conjugated BO<sub>4</sub> groups are less polarized than the  $\pi$ -conjugated B<sub>3</sub>O<sub>6</sub> and BO<sub>3</sub> groups. Aside from the effect of various kinds of anionic groups on the compound SHG response, the microscopic arrangement of anionic groups in the structure does have a significant impact on the compound macroscopic SHG response. Following the investigation, it is clear that, first, the  $1_{\infty}$  [B<sub>2</sub>P<sub>3</sub>O<sub>13</sub>] anionic chain in KNBPO is composed of non- $\pi$ -conjugated BO<sub>4</sub> and PO<sub>4</sub> tetrahedra.

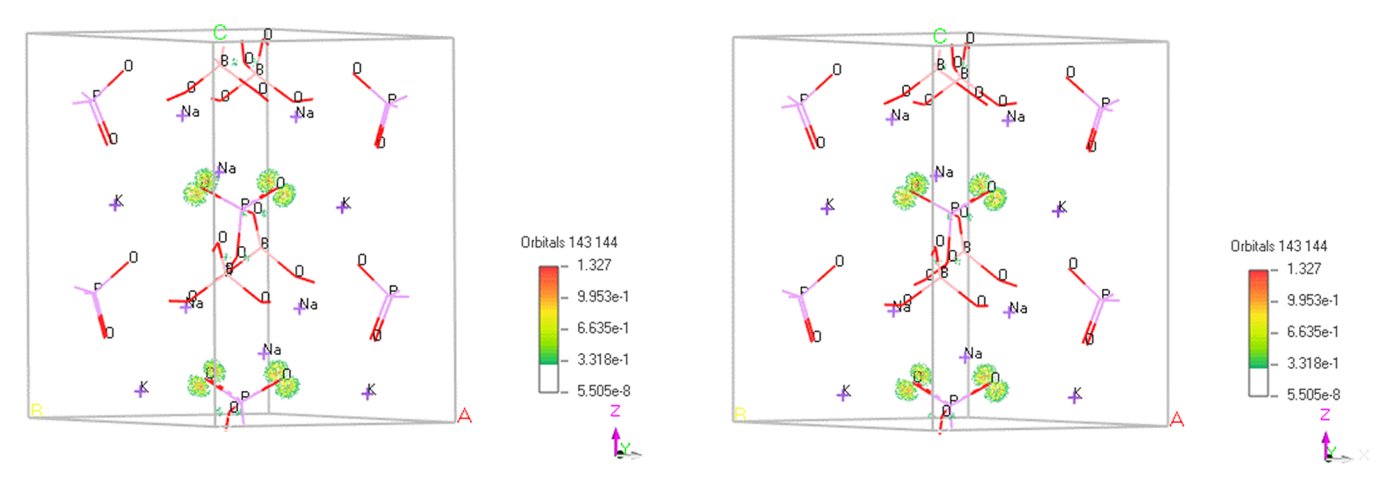


Figure 7. Stereo pair (cross-eyes) view of the orbital density of the two highest occupied bands, with an energy range covering from 0.0 to -0.07 eV below the Fermi level. Note that the probability density is localized on the backbone (P-connected) terminal oxygen.

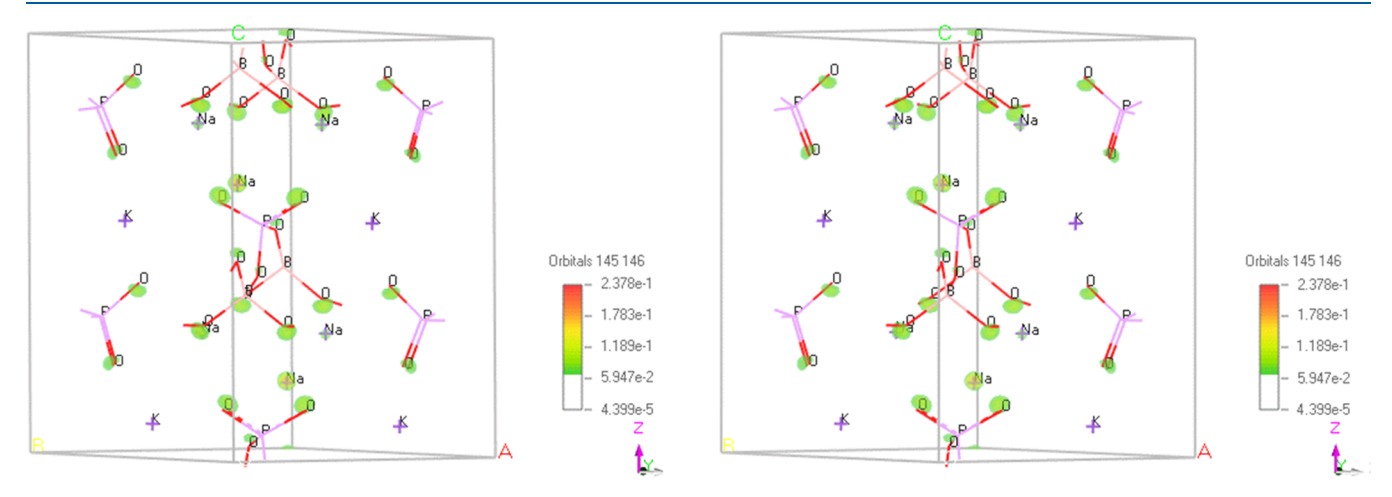


Figure 8. Stereo pair (cross-eyes) view of the orbital density of the two lowest unoccupied bands, with an energy range covering from 5.2 to 6.9 eV above the Fermi level. Note that electrons from terminal and bridging oxygens contribute to those bands.

Second, the forward and reverse alignment of adjacent  $1_{\infty}$  [ $B_2P_3O_{13}$ ] anionic chains along the b-axis weakens the local microscopic polarizability to a certain extent. Certainly, the NLO active groups  $BO_4$  and  $PO_4$  of the non- $\pi$ -conjugated system, together with the unfavorable arrangement of the  $1_{\infty}$  [ $B_2P_3O_{13}$ ] anionic chain to the NLO effect, eventually cause KNBPO to display limited SHG response at the macroscopic level.

**Theoretical Results.** Theoretical computation is an essential approach for deeper understanding of the link between structure and properties. We investigate the electronic structure of KNBPO at the atomic level using the method mentioned in the previous session.

The calculated band structure indicates that both the valence band (VB) maximum and the conduction band (CB) minimum of KNBPO appear at the  $\Gamma$  point (Figure 6a), so it is a direct band gap compound with a band gap value of 5.185 eV. According to the density of states (DOS) and partial density of states (PDOS) plots (Figure 6b), the orbitals near cations K and Na are mostly positioned deep in the VB below -10 eV. The B 2p, P 3p, and O 2p orbitals display clear interhybridization in the VB range from -10 to 0 eV, suggesting that the contribution in this VB area is mostly from the B-O and P-O units. To identify the most important orbitals at two sides of the band gap, we plot the sum orbital densities of the

two highest occupied VBs and the two lowest unoccupied CBs, as shown in Figures 7 and 8. It turns out that VB maximum is mainly made of P-connected terminal oxygen on the continuous backbone, but not those similar at the side chain, whereas the CB minimum is more dispersed to distribute over cation Na and all bridging and terminal oxygen. The strongest density originates from Na ion sites, indicating Na cations may play an important role in optical processes.

In the theoretical research, we also calculated the linear and NLO properties of KNBPO. The three independent SHG coefficients  $d_{31}$ ,  $d_{32}$ , and  $d_{33}$  are predicted to be 0.159, 0.121, and -0.19 pm/V, respectively. The calculated and the experimental SHG coefficients are almost identical when compared to the  $d_{36}$  (0.39 pm/V) value of KDP.<sup>66</sup> With calculated birefringence being ~0.011@1064 nm, the value is not in a typical suitable range (0.05-0.1) for implementing phase matching. The calculated refractive index dispersion curve indicates that  $n_z > n_x > n_y$  (Figure 9), and it is possible to obtain the shortest  $n_v(\omega) = n_z(2\omega)$  at 514 nm, demonstrating that the shortest phase-matching wavelength of KNBPO is 514 nm. Although the birefringence of KNBPO is small, it still maintains phase-matching capacity under 1064 nm laser wavelength, which is consistent with the experimental results. Combining theoretical calculations and the anionic group theory, we speculate that, for KNBPO, its optical properties

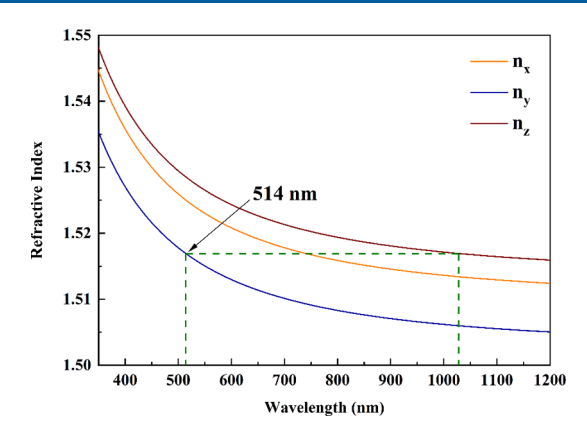


Figure 9. Calculated refractive index dispersion curve for KNBPO.

may be mainly determined by  $BO_4$  and  $PO_4$  units, a conclusion similar to that of Yang et al.<sup>42</sup> Due to the small optical anisotropy of the  $BO_4$  and  $PO_4$  units and their arrangement in the structure that is not conducive to the large SHG response, KNBPO finally has a small birefringence and a small nonlinear coefficient.

#### CONCLUSIONS

In conclusion, the noncentrosymmetric alkali metal borophosphate KNBPO can be obtained by a high-temperature melting method, and its one-dimensional structure is composed of a FBU  $1_{\infty}$  [B<sub>2</sub>P<sub>3</sub>O<sub>13</sub>] chain that is made up of BO<sub>4</sub> and PO<sub>4</sub> tetrahedra joined by corner share, with K and Na orderly embedded between one-dimensional FBU chains. KNBPO has high reflectance over a wide range, and its UV cut-off edge is below 186 nm. As a congruent melting compound, KNBPO has good thermal stability with almost no weight loss during the heating process. According to the DSC characterization, it has a medium melting point of 673 °C. KNBPO can achieve type-I phase matching, but because the one-dimensional FBU B<sub>2</sub>P<sub>3</sub>O<sub>13</sub> group is not placed in the most advantageous pattern for nonlinear effects, its SHG effect is ultimately only 0.42 × KDP. The DFT calculation associated with the experimental structure shows that the small SHG coefficient of KNBPO derives from the unfavorable arrangement of the B<sub>2</sub>P<sub>3</sub>O<sub>13</sub> group. In other words, the emergence of KNBPO provides a particular reference value for researchers of related materials as well as a viable candidate for UV and even deep UV-applied materials.

#### ASSOCIATED CONTENT

#### Supporting Information

The Supporting Information is available free of charge at https://pubs.acs.org/doi/10.1021/acs.inorgchem.2c04499.

Element content and distribution;  $1_{\infty}$  [B<sub>2</sub>P<sub>3</sub>O<sub>13</sub>] chainlayer skeleton structure of KNBPO and its related compounds; PXRD patterns before and after melting; exact atomic coordinates and equivalent isotropic temperature factors; and selected bond lengths (PDF)

#### **Accession Codes**

CCDC 2173985 contains the supplementary crystallographic data for this paper. These data can be obtained free of charge via <a href="www.ccdc.cam.ac.uk/data\_request/cif">www.ccdc.cam.ac.uk/data\_request/cif</a>, or by emailing data\_request@ccdc.cam.ac.uk, or by contacting The Cambridge Crystallographic Data Centre, 12 Union Road, Cambridge CB2 1EZ, UK; fax: +44 1223 336033.

#### AUTHOR INFORMATION

#### **Corresponding Author**

Jiyong Yao — Beijing Center for Crystal Research and Development, Key Lab of Functional Crystals and Laser Technology, Technical Institute of Physics and Chemistry, Chinese Academy of Sciences, Beijing 100190, P. R. China; Center of Materials Science and Optoelectronics Engineering, University of Chinese Academy of Sciences, Beijing 100049, P. R. China; ⊚ orcid.org/0000-0002-4802-5093; Email: jyao@mail.ipc.ac.cn

#### **Authors**

Wenhao Liu — Beijing Center for Crystal Research and Development, Key Lab of Functional Crystals and Laser Technology, Technical Institute of Physics and Chemistry, Chinese Academy of Sciences, Beijing 100190, P. R. China; Center of Materials Science and Optoelectronics Engineering, University of Chinese Academy of Sciences, Beijing 100049, P. R. China; University of Chinese Academy of Sciences, Beijing 100049, P. R. China

Ming-Hsien Lee – Department of Physics, Tamkang University, New Taipei 25137, Taiwan; ⊙ orcid.org/0000-0003-3956-181X

Ruixin Guo — Beijing Center for Crystal Research and Development, Key Lab of Functional Crystals and Laser Technology, Technical Institute of Physics and Chemistry, Chinese Academy of Sciences, Beijing 100190, P. R. China; Center of Materials Science and Optoelectronics Engineering, University of Chinese Academy of Sciences, Beijing 100049, P. R. China

Complete contact information is available at: https://pubs.acs.org/10.1021/acs.inorgchem.2c04499

#### Notes

The authors declare no competing financial interest.

#### ACKNOWLEDGMENTS

This work was supported by the National Natural Science Foundation of China (nos. 22175190 and 51890862).

#### REFERENCES

- (1) Brabec, T.; Krausz, F. Intense Few-Cycle Laser Fields: Frontiers of Nonlinear Optics. *Rev. Mod. Phys.* **2000**, *72*, 545–591.
- (2) Yap, C. Y.; Chua, C. K.; Dong, Z. L.; Liu, Z. H.; Zhang, D. Q.; Loh, L. E.; Sing, S. L. Review of Selective Laser Melting: Materials and Applications. *Appl. Phys. Rev.* **2015**, *2*, No. 041101.
- (3) Kogelnik, H.; Li, T. Laser Beams and Resonators. *Appl. Opt.* **1966**, *5*, 1550–1567.
- (4) Yao, J.; Mei, D.; Bai, L.; Lin, Z.; Yin, W.; Fu, P.; Wu, Y. BaGa<sub>4</sub>Se<sub>7</sub>: A New Congruent-Melting IR Nonlinear Optical Material. *Inorg. Chem.* **2010**, 49, 9212–9216.
- (5) Kang, L.; Liang, F.; Jiang, X.; Lin, Z.; Chen, C. First-Principles Design and Simulations Promote the Development of Nonlinear Optical Crystals. *Acc. Chem. Res.* **2020**, 53, 209–217.
- (6) Mutailipu, M.; Zhang, M.; Yang, Z.; Pan, S. Targeting the Next Generation of Deep-Ultraviolet Nonlinear Optical Materials: Expanding from Borates to Borate Fluorides to Fluorooxoborates. *Acc. Chem. Res.* **2019**, *52*, 791–801.
- (7) Tran, T. T.; Yu, H.; Rondinelli, J. M.; Poeppelmeier, K. R.; Halasyamani, P. S. Deep Ultraviolet Nonlinear Optical Materials. *Chem. Mater.* **2016**, 28, 5238–5258.
- (8) Wu, C.; Yang, G.; Humphrey, M. G.; Zhang, C. Recent Advances in Ultraviolet and Deep-Ultraviolet Second-Order Nonlinear Optical Crystals. *Coord. Chem. Rev.* **2018**, *375*, 459–488.

- (9) Xia, Y.; Chen, C.; Tang, D.; Wu, B. New Nonlinear Optical Crystals for UV and VUV Harmonic Generation. *Adv. Mater.* **1995**, 7, 79–81.
- (10) Chen, C.; Wu, Y.; Jiang, A.; Wu, B.; You, G.; Li, R.; Lin, S. New Nonlinear-Optical Crystal: LiB<sub>3</sub>O<sub>5</sub>. *J. Opt. Soc. Am. B* **1989**, *6*, 616–621.
- (11) Chen, C.; Wu, B.; Jiang, A.; You, G. A New-Type Ultraviolet SHG Crystal— $\beta$ -BaB<sub>2</sub>O<sub>4</sub>. Sci. China Ser. B: Chem. **1985**, 28, 235.
- (12) Wu, Y.; Sasaki, T.; Nakai, S.; Yokotani, A.; Tang, H.; Chen, C.  $CsB_3O_5$ : A New Nonlinear Optical Crystal. *Appl. Phys. Lett.* **1993**, *62*, 2614–2615.
- (13) Mori, Y.; Kuroda, I.; Nakajima, S.; Sasaki, T.; Nakaj, S. New Nonlinear Optical Crystal: Cesium Lithium Borate. *Appl. Phys. Lett.* **1995**, *67*, 1818–1820.
- (14) Zaitseva, N.; Carman, L. Rapid Growth of KDP-Type Crystals. *Prog. Cryst. Growth Charact. Mater.* **2001**, 43, 1–118.
- (15) Stolzenberger, R. A. Nonlinear Optical Properties of Flux Growth KTiOPO<sub>4</sub>. Appl. Opt. 1988, 27, 3883–3886.
- (16) Miller, R. C. Optical Second Harmonic Generation in Piezoelectric Crystals. *Appl. Phys. Lett.* **1964**, *5*, 17–19.
- (17) Chen, C.; Wang, Y.; Wu, B.; Wu, K.; Zeng, W.; Yu, L. Design and Synthesis of an Ultraviolet-Transparent Nonlinear Optical Crystal Sr<sub>2</sub>Be<sub>2</sub>B<sub>2</sub>O<sub>7</sub>. *Nature* **1995**, 373, 322–324.
- (18) Li, Z.; Lin, Z.; Wu, Y.; Fu, P.; Wang, Z.; Chen, C. Crystal Growth, Optical Properties Measurement, and Theoretical Calculation of BPO<sub>4</sub>. *Chem. Mater.* **2004**, *16*, 2906–2908.
- (19) Kniep, R.; Engelhardt, H.; Hauf, C. A First Approach to Borophosphate Structural Chemistry. *Chem. Mater.* **1998**, *10*, 2930–2934.
- (20) Ewald, B.; Huang, Y.; Kniep, R. Structural Chemistry of Borophosphates, Metalloborophosphates, and Related Compounds. Z. Anorg. Allg. Chem. 2007, 633, 1517.
- (21) Li, M.; Verena-Mudring, A. New Developments in the Synthesis, Structure, and Applications of Borophosphates and Metalloborophosphates. *Cryst. Growth Des.* **2016**, *16*, 2441–2458.
- (22) Mutailipu, M.; Poeppelmeier, K. R.; Pan, S. Borates: A Rich Source for Optical Materials. *Chem. Rev.* **2021**, *121*, 1130–1202.
- (23) Mutailipu, M.; Xie, Z.; Su, X.; Zhang, M.; Wang, Y.; Yang, Z.; Janjua, M. R. S. A.; Pan, S. Chemical Cosubstitution-Oriented Design of Rare-Earth Borates as Potential Ultraviolet Nonlinear Optical Materials. *J. Am. Chem. Soc.* **2017**, *139*, 18397–18405.
- (24) Liu, W.; Liu, X.; Meng, X.; Li, C.; Sun, M.; Lin, Z.; Yao, J. Two Non-Centrosymmetric Scandium Borate Nonlinear Optical Crystals Containing the B<sub>5</sub>O<sub>10</sub> Anion Group. *J. Alloys Compd.* **2022**, 902, No. 163832.
- (25) Hellwig, H.; Liebertz, J.; Bohatý, L. Exceptional Large Nonlinear Optical Coefficients in the Monoclinic Bismuth Borate  $BiB_3O_6$  (BIBO). Solid State Commun. 1998, 109, 249–251.
- (26) Li, X.; Yang, L.; Zhu, Z.; Wang, X.; Chen, P.; Huang, S.; Wei, X.; Cai, G.; Manuel, P.; Yang, S.; Lin, J.; Kuang, X.; Sun, J. Borates as a new direction in the design of oxide ion conductors. *Sci. China Mater.* **2022**, *65*, 2737–2745.
- (27) Legrand, A. P.; Sfihi, H.; Lequeux, N.; Lemaître, J. <sup>31</sup>P Solid-State NMR Study of the Chemical Setting Process of a Dual-Paste Injectable Brushite Cements. *J. Biomed. Mater. Res., Part B* **2009**, *91B*, 46–54.
- (28) Deng, Y.; Huang, L.; Dong, X.; Wang, L.; Ok, K. M.; Zeng, H.; Lin, Z.; Zou, G.  $K_2Sb(P_2O_7)F$ : Cairo Pentagonal Layer with Bifunctional Genes Reveal Optical Performance. *Angew. Chem., Int. Ed.* **2020**, *59*, 21151–21156.
- (29) Qian, Z.; Wu, H.; Yu, H.; Hu, Z.; Wang, J.; Wu, Y. Synthesis, Structure and Characterization of Three New Mg-Containing Phosphates with Deep-UV Cut-Off Edges. *New J. Chem.* **2020**, *44*, 6771–6777.
- (30) Zhang, W.; Cheng, W.; Zhang, H.; Geng, L.; Li, Y.; Lin, C.; He, Z. Syntheses and Characterizations of  $Cs_2Cr_3(BP_4O_{14})(P_4O_{13})$  and  $CsFe(BP_3O_{11})$  Compounds with Novel Borophosphate Anionic Partial Structures. *Inorg. Chem.* **2010**, *49*, 2550–2556.

- (31) Zhao, S.; Yang, X.; Yang, Y.; Kuang, X.; Lu, F.; Shan, P.; Sun, Z.; Lin, Z.; Hong, M.; Luo, J. Non-Centrosymmetric RbNaMgP $_2O_7$  with Unprecedented Thermo-Induced Enhancement of Second Harmonic Generation. *J. Am. Chem. Soc.* **2018**, *140*, 1592–1595.
- (32) Yang, X.; Zhao, S.; Geng, S.; Yang, L.; Huang, Q.; Kuang, X.; Luo, J.; Xing, X. Structural Origin of Thermally Induced Second Harmonic Generation Enhancement in RbNaMgP<sub>2</sub>O<sub>7</sub>. *Chem. Mater.* **2019**, *31*, 9843–9849.
- (33) Pan, S.; Wu, Y.; Fu, P.; Zhang, G.; Li, Z.; Du, C.; Chen, C. Growth, Structure, and Properties of Single Crystals of SrBPO<sub>5</sub>. *Chem. Mater.* **2003**, *15*, 2218.
- (34) Wang, Y.; Pan, S.; Zhang, M.; Han, S.; Su, X.; Dong, L. Synthesis, Crystal Growth and Characterization of a New Noncentrosymmetric Borophosphate: RbPbBP<sub>2</sub>O<sub>8</sub>. CrystEngComm **2013**, 15, 4956.
- (35) Schmidt, M.; Ewald, B.; Prots, Y.; Cardoso-Gil, R.; Armbrüster, M.; Loa, I.; Zhang, L.; Huang, Y.; Schwarz, U.; Kniep, R. Growth and Characterization of BPO<sub>4</sub> Single Crystals. *Z. Anog. Allg. Chem.* **2004**, 630, 655–662.
- (36) Bauer, H. Über eine Reihe isotyper Erdalkaliboratphosphate und -arsenate vom Typus 2 MeO·X<sub>2</sub>O<sub>5</sub>·B<sub>2</sub>O<sub>3</sub>. Z. Anorg. Allg. Chem. **1965**, 337, 183–190.
- (37) Pan, S.; Wu, Y.; Fu, P.; Zhang, G.; Wang, G.; Guan, X.; Chen, C. The Growth of  $BaBPO_5$  Crystals From  $Li_4P_2O_7$  Flux. J. Cryst. Growth 2002, 236, 613–616.
- (38) Zhao, D.; Cheng, W.; Zhang, H.; Huang, S.; Xie, Z.; Zhang, W.; Yang, S. KMBP $_2$ O $_8$ (M = Sr, Ba): A New Kind of Noncentrosymmetry Borophosphate with the Three-Dimensional Diamond-Like Framework. *Inorg. Chem.* **2009**, 48, 6623–6629.
- (39) Li, Z.; Wu, Y.; Fu, P.; Pan, S.; Wang, G.; Cheng, C. Crystal Growth of Na<sub>5</sub>[B<sub>2</sub>P<sub>3</sub>O<sub>13</sub>]. *Chem. Lett.* **2002**, *31*, 560–561.
- (40) Li, H.; Zhao, Y.; Pan, S.; Wu, H.; Yu, H.; Zhang, F.; Yang, Z.; Poeppelmeier, K. R. Synthesis and Structure of  $KPbBP_2O_8 A$  Congruent Melting Borophosphate with Nonlinear Optical Properties. *Eur. J. Inorg. Chem.* **2013**, 2013, 3185–3190.
- (41) Shi, Y.; Pan, S.; Dong, X.; Wang, Y.; Zhang, M.; Zhang, F.; Zhou, Z. Na<sub>3</sub>Cd<sub>3</sub>B(PO<sub>4</sub>)<sub>4</sub>: A New Noncentrosymmetric Borophosphate with Zero-Dimensional Anion Units. *Inorg. Chem.* **2012**, *51*, 10870–10875.
- (42) Yang, Y.; Gong, P.; Huang, Q.; Song, G.; Liu, X.; Lin, Z.  $KNa_4B_2P_3O_{13}$ : A Deep-Ultraviolet Transparent Borophosphate Exhibiting Second-Harmonic Generation Response. *Inorg. Chem.* **2019**, *58*, 8918–8921.
- (43) Yu, S.; Wu, H.; Yu, H.; Hu, Z.; Wang, J.; Wu, Y.  $NH_4(B_6PO_{10}(OH)_4)\cdot H_2O$ : Exhibiting the Largest Birefringence in Borophosphates. *Chem. Commun.* **2022**, *58*, 2834–2837.
- (44) Cheng, B.; Li, Z.; Chu, Y.; Tudi, A.; Mutailipu, M.; Zhang, F.; Yang, Z.; Pan, S.  $(NH_4)_3B_{11}PO_{19}F_3$ : A Deep-UV Nonlinear Optical Crystal with Unique  $[B_5PO_{10}F]_{\infty}$  Layers. *Natl. Sci. Rev.* **2022**, *9*, nwac110.
- (45) Zhang, W.; Huang, J.; Han, S.; Yang, Z.; Pan, S. Enhancement of Birefringence in Borophosphate Pushing Phase-Matching into the Short-Wavelength Region. J. Am. Chem. Soc. 2022, 144, 9083–9090.
- (46) Huang, Y.; Wu, L.; Wu, X.; Li, L.; Chen, L.; Zhang, Y. Pb<sub>2</sub>B<sub>5</sub>O<sub>9</sub>I: An Iodide Borate with Strong Second Harmonic Generation. *J. Am. Chem. Soc.* **2010**, *132*, 12788–12789.
- (47) Zhang, W.; Cheng, W.; Zhang, H.; Geng, L.; Lin, C.; He, Z. A Strong Second-Harmonic Generation Material Cd<sub>4</sub>BiO(BO<sub>3</sub>)<sub>3</sub> Originating from 3-Chromophore Asymmetric Structures. *J. Am. Chem. Soc.* **2010**, *132*, 1508–1509.
- (48) Lei, B.; Jing, Q.; Yang, Z.; Zhang, B.; Pan, S. Anomalous Second-Harmonic Generation Response in SrBPO<sub>5</sub> and BaBPO<sub>5</sub>. *J. Mater. Chem. C* **2015**, *3*, 1557–1566.
- (49) Sheldrick, G. SHELXT Integrated Space-Group and Crystal-Structure Determination. *Acta Crystallogr.*, A **2015**, 71, 3–8.
- (50) Dolomanov, O.; Bourhis, L.; Gildea, R.; Howard, J.; Puschmann, H. OLEX2: A Complete Structure Solution, Refinement and Analysis Program. *J. Appl. Crystallogr.* **2009**, *42*, 339–341.

- (51) Sheldrick, G. Crystal Structure Refinement with SHELXL. *Acta Crystallogr.*, C **2015**, 71, 3–8.
- (52) Kurtz, S. K.; Perry, T. T. A Powder Technique for the Evaluation of Nonlinear Optical Materials. *J. Appl. Phys.* **1968**, 39, 3798–3813.
- (53) Clark, S. J.; Segall, M. D.; Pickard, C. J.; Hasnip, P. J.; Probert, M. I. J.; Refson, K.; Payne, M. C. First Principles Methods Using CASTEP. Z. Kristallogr. Cryst. Mater. 2005, 220, 567–570.
- (54) Kohn, W.; Sham, L. J. Self-Consistent Equations Including Exchange and Correlation Effects. *Phys. Rev.* **1965**, *140*, A1133–A1138
- (55) Hohenberg, P.; Kohn, W. Inhomogeneous Electron Gas. *Phys. Rev.* **1964**, *136*, B864–B871.
- (56) Payne, M.; Teter, M.; Allan, D.; Arias, T.; Joannopoulos, J. Iterative Minimization Techniques for *ab initio* Total-Energy Calculations: Molecular Dynamics and Conjugate Gradients. *Rev. Mod. Phys.* **1992**, *64*, 1045–1097.
- (57) Medvedev, M.; Bushmarinov, I.; Sun, J.; Perdew, J.; Lyssenko, K. Density Functional Theory is Straying from the Path Toward the Exact Functional. *Science* **2017**, *355*, 49–52.
- (58) Monkhorst, H. J.; Pack, J. D. Special Points for Brillouin-Zone Integrations. *Phys. Rev. B* **1976**, *13*, 5188–5192.
- (59) Rappe, A. M.; Rabe, K. M.; Kaxiras, E.; Joannopoulos, J. D. Optimized Pseudopotentials. *Phys. Rev. B* **1990**, *41*, 1227–1230.
- (60) Kleinman, L.; Bylander, D. M. Efficacious Form for Model Pseudopotentials. *Phys. Rev. Lett.* **1982**, *48*, 1425–1428.
- (61) Refson, K.; Tulip, P. R.; Clark, S. J. Variational Density-Functional Perturbation Theory for Dielectrics and Lattice Dynamics. *Phys. Rev. B* **2006**, *73*, No. 155114.
- (62) Miwa, K. Prediction of Raman Spectra with Ultrasoft Pseudopotentials. *Phys. Rev. B* **2011**, *84*, No. 094304.
- (63) Wang, Y.; Pan, S.; Shi, Y. Further Examples of the P-O-P Connection in Borophosphates: Synthesis and Characterization of Li<sub>2</sub>Cs<sub>2</sub>B<sub>2</sub>P<sub>4</sub>O<sub>15</sub>, LiK<sub>2</sub>BP<sub>2</sub>O<sub>8</sub>, and Li<sub>3</sub>M<sub>2</sub>BP<sub>4</sub>O<sub>14</sub> (M=K, Rb). *Chem. Eur. J.* **2012**, *18*, 12046–12051.
- (64) Li, Z.; Wu, Y.; Fu, P.; Pan, S.; Lin, Z.; Chen, C. Czochralski Crystal Growth and Properties of  $Na_s[B_2P_3O_{13}]$ . *J. Cryst. Growth* **2003**, 255, 119–122.
- (65) Chen, C.; Wu, Y.; Li, R. The Anionic Group Theory of the Non-Linear Optical Effect and its Applications in the Development of New High-Quality NLO Crystals in the Borate Series. *Int. Rev. Phys. Chem.* **1989**, *8*, 65–91.
- (66) Zhang, B.; Tikhonov, E.; Xie, C.; Yang, Z.; Pan, S. Prediction of Fluorooxoborates with Colossal Second Harmonic Generation (SHG) Coefficients and Extremely Wide Band Gaps: Towards Modulating Properties by Tuning the BO<sub>3</sub>/BO<sub>3</sub>F Ratio in Layers. *Angew. Chem., Int. Ed.* **2019**, *58*, 11726–11730.

### **□** Recommended by ACS

Mixed Alkali Metal and Alkaline Earth Metal Scandium Borate Birefringence Material with Layered Structure and Short Ultraviolet Cutoff Edge

Wenhao Liu, Jiyong Yao, et al.

JUNE 15, 2023

INORGANIC CHEMISTRY

READ 🗹

Structural Motif Cosubstitution Strategy for Designing Fluoroaluminoborate with the  $Sr_2Be_2B_2O_7$ -Type Double-Layered Structure

Jiahao Jiao, Min Zhang, et al.

MARCH 03, 2023

INORGANIC CHEMISTRY

READ 🗹

Sharp Enhancement of Birefringence in Antimony Oxalates Achieved by the Cation-Anion Synergetic Interaction Strategy

Die Zhang, Guohong Zou, et al.

JULY 27, 2022

INORGANIC CHEMISTRY

READ 🗹

 $AKTeO_2(CO_3) \ (A=Li, Na) \hbox{: The First Carbonatotellurites} \\ Featuring a Zero-Dimensional \ [Te_2C_2O_{10}]^4 \ Cluster \ and \ a \\ Wide Band Gap$ 

Peng-Fei Chen, Jiang-Gao Mao, et al.

APRIL 20, 2023

INORGANIC CHEMISTRY

READ 🗹

Get More Suggestions >